Journal of Power Sources 601 (2024) 234285

Contents lists available at ScienceDirect

Journal of Power Sources

journal homepage: www.elsevier.com/locate/jpowsour

Rational design of trifunctional conductive binder for high-performance Si anodes in lithium-ion batteries

Wenhui Geng [a], Xinmeng Hu [a], Qinhua Zhou [a], Yinhang Zhang [a,*], Bin He [b,c], Zhiliang Liu [b,c], Kuikui Xiao [a,**], Dong Cai [a,***], Shuo Yang [a], Huagui Nie [a], Zhi Yang [a,****]

[a] Key Laboratory of Carbon Materials of Zhejiang Province, College of Chemistry and Materials Engineering, Wenzhou University, Wenzhou, 325035, China
[b] Harbin Wanxin Graphite Valley Tech Co., Ltd., Harbin, 150029, China
[c] Zhejiang Wanxin Olefin Carbon Technology Co., Ltd., Wenzhou, 325062, China

HIGHLIGHTS

- Lithiated PAA could ameliorate the transport performance of lithium ions.
- Constructed double conductive network realized the formation of electron seepage and molecular scale electron coupling.
- The optimized mechanical performances realized the structural and cycling stability of the anode.

ARTICLE INFO

Keywords:
Lithium-ion batteries
Si anode
Binder
Conductive

ABSTRACT

Silicon (Si) has been regarded as a candidate for high-energy-density lithium-ion batteries (LIBs) because of its excellent specific capacity. Binders, as an essential component in Si anodes, play a key role in enhancing the electrochemical performance of LIBs. In this study, a multifunctional binder named LP19 simultaneously possessing high electron conductivity, high Li-ion conductivity as well as ameliorative mechanical performances was synthesized by assembling the lithiated PAA (LiPAA) and highly conductive PEDOT:PSS molecules. The lithiation treatment of PAA is conducive to the transport of lithium ions, while the double conductive network constructed by conductive PEDOT:PSS and Super P guarantees the stable electric connectivity during lithiation and delithiation processes. Moreover, the optimization of the internal configuration of the molecules realizes the structural and cycling stability of the Si anode. As a consequence, the Si anode utilizing this binary and multifunctional conductive binder demonstrated pronounced cycling stability (2165 mAh g^{-1} after 200 cycles) and rate performance (1750 mAh g^{-1} at 8.0 A g^{-1}). This work provided a novel design strategy of polymeric binders to promote progress toward high-performance LIBs.

1. Introduction

Lithium-ion batteries (LIBs) have been widely used in portable electronic devices, electric vehicles and energy storage products, designing and developing LIBs with high energy density and excellent electrochemical performance is of paramount importance [1–3]. Silicon (Si) has an excellent theoretical specific capacity of 4200 mAh g^{-1}, which is 10 times larger than that of the traditional graphite anode (372 mAh g^{-1}), thus it has been recognized as the most potential alternative of traditional graphite anodes [4–8]. However, issues caused by the large volumetric variation of silicon in the process of lithiation and delithiation, including particle pulverization, active material shedding and repeated growth of the SEI layer, limit the commercialization of silicon anode materials [9–11].

Tremendous efforts have been made to develop Si-based active materials to accommodate these issues, mostly through engineering Si materials [12–17], which can relieve the influence of immense volume expansion and improve the lithium diffusion inside the electrode.

* Corresponding authors.
** Corresponding author.
*** Corresponding authors.
**** Corresponding author.
E-mail addresses: bank0719@163.com (Y. Zhang), xiaokuikuihnu@163.com (K. Xiao), caidong@wzu.edu.cn (D. Cai), yang201079@126.com (Z. Yang).

https://doi.org/10.1016/j.jpowsour.2024.234285
Received 25 October 2023; Received in revised form 11 February 2024; Accepted 28 February 2024

However, these approaches are complicated, high-cost and environmentally unfriendly [18,19]. In contrast, binder modification is considered to be one of the most promising strategies for solving the issues of Si-based anode materials [20–22]. Although some mainstream binders, such as polyacrylic acid (PAA), carboxymethyl cellulose (CMC) and styrene butadiene rubber (SBR) have been proved to exhibit better binding performances than that of the conventional polyvinylidene fluoride (PVDF), their linear structure allows them to be susceptible to sliding upon the sustaining volume expansion of Si-based anode materials. Consequently, crosslinked binders were developed to inhibit the slide phenomenon, thus ensuring the structural stability of the Si-based anode materials effectively [23–25]. For example, a crosslinked network formed by the thermal condensation of –OH of CMC and –COOH of PAA was synthesized in Koo's study [26]. Nanosized Si particles with the prepared 3D interconnected network binder exhibited a high reversible capacity of over 2000 mAh g^{-1} after 100 cycles and maintained superior capacity of 1500 mAh g^{-1} for the high current density of 30 A g^{-1} at 60 °C. The utilization of crosslinked binders has effectively ameliorated the electrochemical performances; however, these insulating binders severely inhibit electron transport between active materials. It is known that traditional conductive additives such as acetylene black are easy to lose direct contact with the active materials by large volume expansion during cycling processes, leading to fractured electric connections and rapid battery capacity attenuation.

To form stable electron connections among active particles, meticulously designed conductive binders have progressively emerged as a promising alternative and they should be given due attention. Conductive binders can be used as both conductive agent and binder simultaneously, allowing the construction of stable bridges of electronic connections in anode, thus guaranteeing the structural integrity and the electrochemical activity. Su et al. [27] successfully synthesized a multifunctional polymer binder named as PPTU by hydrogen-bond crosslinking of conductive PEDOT:PSS and stretchable polymer poly (ether-thioureas) (PETU). The Si anode demonstrated excellent cycling stability and rate capacity due to the interweaving conductive and continuous 3D network of prepared binder, which is beneficial to mechanical stability and electron transfer. Pan e al. [28] prepared a novel binder based on a mixture of PAA and PEDOT:PSS to significantly improve the specific capacity and cycling stability of Li–S batteries via the synergistic effect of the different functional groups. The PEDOT:PSS could facilitate the electron transfer and prevent the polysulfide dissolution. PAA improves the solvent system for sulfur cathodes and promotes lithium-ion transfer. Other conductive binders such as polyfluorene and polyaniline were also designed for the Si anode, much of these works were focused on synthesizing high conductive binders [29–32]. Some other factors, such as good mechanical properties, strong interface compatibility, and transport facilitation of Li^+ are also the key considerations in creating a suitable binder for Si anode. Of particular note, the charge transfer capacity within the binder molecules and the charge transfer rate at the interface between the binder and the active particles are two crucial factors for a stable charge transfer inside the binder [33].

In this work, we successfully synthesized a polymer binder for Si anode simultaneously possessing high electron conductivity, high Li-ion conductivity as well as ameliorative mechanical performances. The binder is prepared by assembling lithiated PAA (LiPAA) and highly conductive PEDOT:PSS via a hydrogen-bonding crosslinking strategy. The purpose of lithiation of PAA is to ameliorate the transport performance of lithium ions. The double conductive network constructed by PEDOT:PSS and conductive Super P can not only realize the formation of electron seepage between Super P particles and active materials on the macro scale, but also form the molecular scale electron coupling at the interface of conductive binder and active particles on the micro scale, thus enhancing the rate performance and energy density of the anode. Moreover, due to the optimization of the internal configuration of the molecules and the formation of large amounts of hydrogen bonds, the mechanical properties of the composite binders are optimized, realizing the structural and cycling stability of the anode. The binary binder exhibited pronounced electrochemical properties and it will also promote the development of the next generation of high-energy-density LIBs.

2. Results and discussion

Fig. 1 illustrates the action mechanism of traditional PAA, conductive PEDOT:PSS and the as-synthesized LP binders in the Si electrode during working. Due to the one-dimensional linear structure, the PAA molecules are easily slipped from the silicon surface, thus affecting the structural integrity and electric connectivity (Fig. 1a). Although conductive PEDOT:PSS can maintain a superior electric connectivity in the electrode, their brittleness caused by the intrinsic crystallinity can affect the mechanical stability of the Si electrode (Fig. 1b). Consequently, a binary network by combining lithiated PAA and conductive PEDOT:PSS simultaneously possessing high electron conductivity, high Li-ion conductivity as well as optimized mechanical performances was designed and the working mechanism was presented in Fig. 1c. The lithiation of PAA, the double conductive network constructed by PEDOT:PSS and conductive Super P and the optimization of the internal configuration of the molecules enable a high Li-ion transport performance, stable electric connectivity and mechanical stability of electrodes during cycling, respectively.

The rate capability reflecting the power performance and internal resistance of an electrode was examined in terms of the LP19 binder with different ratio of PEDOT:PSS to LiPAA. As can be seen in Fig. S1, the Si@LP19 exhibited the best rate performance and high capacities of 4110, 2988, 2642, 2253 and 1750 mAh g^{-1} were obtained under current densities of 0.5 A g^{-1}, 1.0 A g^{-1}, 2.0 A g^{-1}, 4.0 A g^{-1} and 8.0 A g^{-1}, respectively. It is also worth noting that the specific capacity retrieved to 2824 mAh g^{-1} when the current density quickly returns to 0.5 A g^{-1}, demonstrating a pronounced kinetic performances and excellent structural stability of the Si@LP19 electrode. In view of this result, the electrochemical properties of Si@LP19 would be comprehensively investigated to shed light on its working mechanism and reveal their potential application prospect of this novel conductive binder in this study.

The first galvanostatic profiles examined at a current density of 0.5 A g^{-1} for Si electrodes with binders of LP19, LiPAA and PEDOT:PSS are shown in Fig. 2a and it can be seen the three electrodes present plateaus at 0.45 V for delithiation and 0.12 V for lithiation. The Si@LiPAA electrode exhibited the highest initial coulombic efficiency (ICE) mainly attributed to the lithiation treatment of the binder which facilities the Li^+ transport inside the electrode (Fig. S2) [29]. The Si@LP19 electrode showed a ICE of 72.5%, which is still 16.2% higher than that of the Si@PEDOT:PSS electrode. Achieving a high initial coulombic efficiency ensures that the cell starts with a maximum useable capacity, enhancing the overall efficiency and energy density of the system. The typical cyclic voltammetry (CV) curves of the Si@LP19 electrode under the scanning rate of 0.05 mV s^{-1} between 0.01 and 1.5 V (vs Li/Li^+) were examined for further understanding the effect of the LP19 binder on the electrochemical performances of Si anodes, as shown in Fig. 2b. The peak appearing at 0.12 V in cathodic sweep corresponds to lithiation process from Si to Li_xSi_y phase, while two peaks appearing at 0.37 V and 0.51 V corresponds to the delithiation process from amorphous Li_xSi_y alloys to amorphous Si [27]. Fig. 2c presents the rate performance of the electrodes with different binders at varied current densities from 0.5 A g^{-1} to 8.0 A g^{-1}. Distinctly, the Si@LP19 exhibited the best rate performance. The long-term cycling performance for electrodes with different binders at a low current density of 1.0 A g^{-1} for 200 cycles were conducted and the results were shown in Fig. 2d. The first several cycles should be ascribed to the electrolyte penetration/electrode activation when the cell operated [34]. Compared to the Si@LiPAA and Si@PEDOT:PSS, the Si@LP19 electrode showed a significantly ameliorated

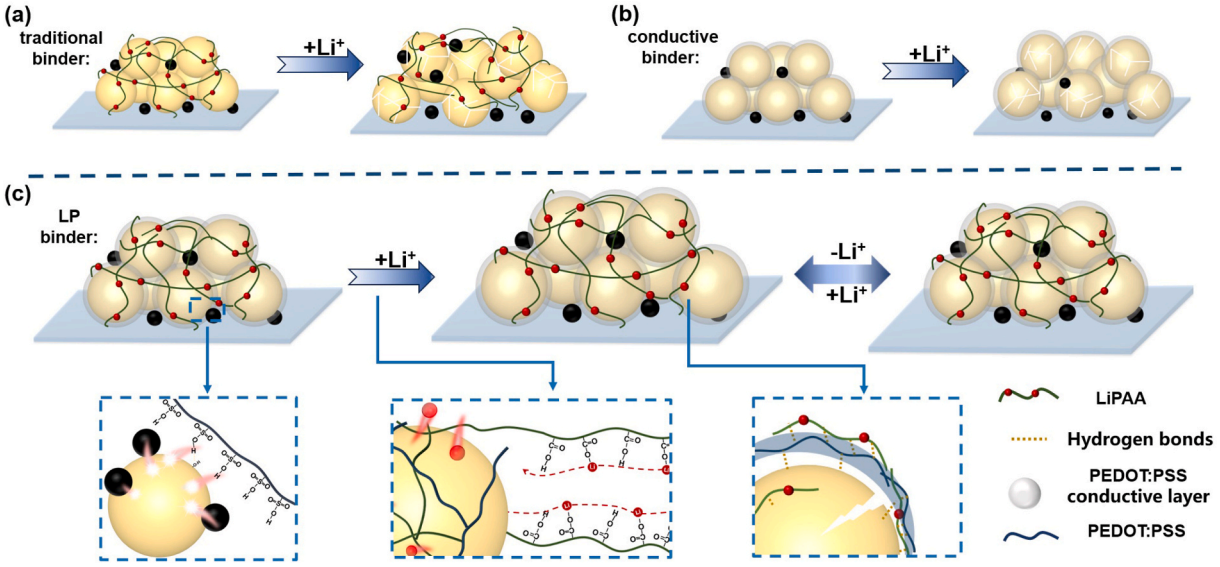

Fig. 1. Schematic illustration of the function mechanism of the (a) traditional binder, (b) conductive binder, and (c) LP binder in Si electrode.

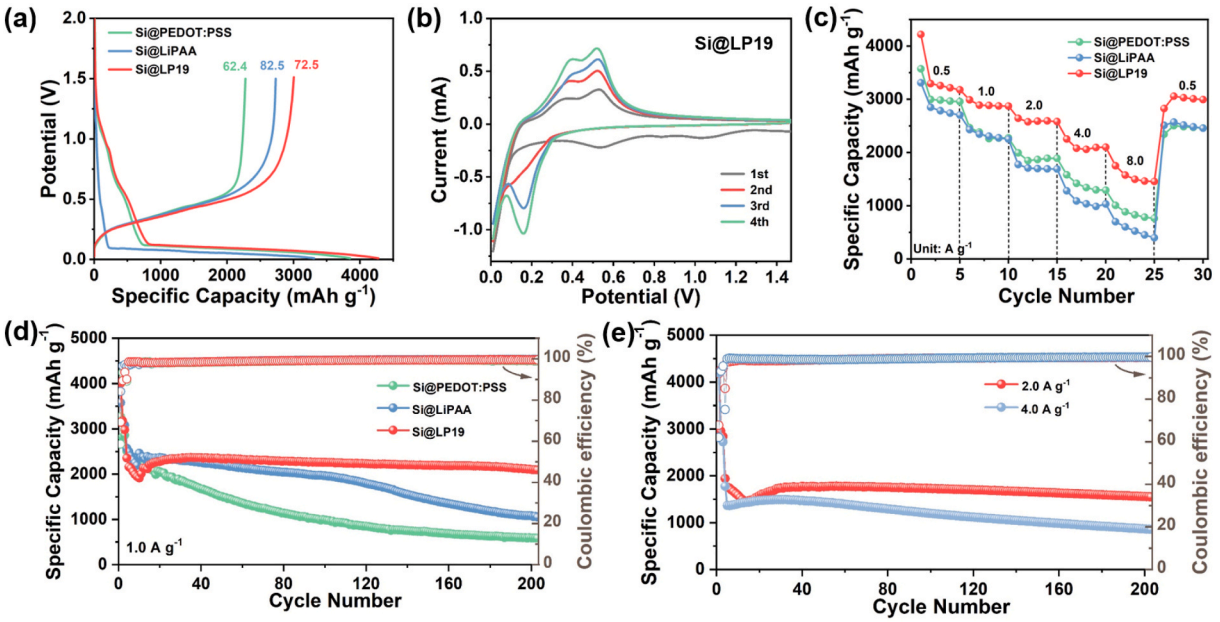

Fig. 2. Characterization of electrochemical performance. (a) The initial charge-discharge capacity-voltage curves at 0.5 A g^{-1}. (b) CV curves of Si@LP19 electrodes at 0.05 mV s^{-1}. (c) Rate performances of electrodes. (d) Cycling stability of electrodes with different binders at a current density of 1.0 A g^{-1}. (e) Cycling performance of Si@LP19 electrodes at current density of 2.0 A g^{-1} and 4.0 A g^{-1}.

cycling performance. The Si@LP19 exhibited an excellent discharge capacity of 2165 mAh g^{-1} after 200 cycles with a high capacity retention ratio of 91.9%, while for those of Si@LiPAA and Si@PEDOT:PSS electrodes, the capacities only reached to 998 and 586 mAh g^{-1} and the capacity retention ratios were 38.8% and 23.4%, respectively, verifying the validity of this novel binder. For comparison, the cycling performance of electrodes using commercial binders, such as PAA and CMC/SBR were also determined and the results were shown in Fig. S3. Both of them showed inferior cycling stability to that of the Si@LP19, further demonstrating the availability of ingenious design of this novel binder. Fig. 2e presents the long-term cycling performance of Si@LP19 electrodes at higher current density of 2.0 A g^{-1} and 4.0 A g^{-1}. It can be seen that the Si@LP19 delivered a stable cycling performance at a current density of 2.0 A g^{-1}, and after 200 cycles, the reversible capacity is 1562 mAh g^{-1}. Even at a larger current density of 4.0 A g^{-1}, the reversible capacity still is 859 mAh g^{-1} after 200 cycles, demonstrating the superior electrochemical stability of this electrode. Cycling performance of the Si@LP19 electrode with loadings of 0.91 mg cm^{-2} and 1.07 mg cm^{-2} are supplied in Fig. S4. Observations indicate that Si@LP19 electrodes, with loadings of 0.91 mg cm^{-2} and 1.07 mg cm^{-2}, retain areal capacities of 1.86 mAh cm^{-2} and 2.35 mAh cm^{-2} at 2.0 A g^{-1} after 50 cycles, respectively. This performance can be attributed to the strong adhesion strength and the double conductive network structure, which maintain electrode integrity, thereby enabling satisfactory cyclability under high current density and mass loading. In addition, the binder was applied to Si/C and cyclic stability tests were conducted at 2.0 A g^{-1} (Fig. S5). The results showed that LP19 binders were more conducive to maintaining the cycling stability of Si/C, with a specific capacity exceeding 600 mAh g^{-1} even after 200 cycles. Electrodes with LiPAA and PEDOT:PSS binders decay rapidly, and from the decay trend,

the deterioration of the PEDOT:PSS binder is more pronounced after 200 cycles.

The contact angle test was carried out to analyze the wettability between electrode and electrolyte (Fig. 3a). In comparison with those of Si@LiPAA and Si@PEDOT:PSS electrodes, the Si@LP19 showed the minimum contact angle of 12.4°, indicating the smallest surface energy, which is beneficial for Li^+ migration. Since the electrolyte composition is the same, the lower surface energy should be attributed to the molecular structure of the LP19 binder. The abundant formation of hydrogen bonds between LiPAA and PEDOT:PSS molecules enhances their polarity, thereby reducing the contact angle. The compatibility between the binder and Si nanoparticles was also determined by contact angle test, and it can be seen in Fig. 3b, the LP19 exhibited the smallest contact angle of 36.7°, indicating the best interface affinity Si and LP19 binder, which is conducive to the mechanical stability of the electrode. The Li-ion diffusion coefficients of the PEDOT:PSS and LP19 binder were determined using the galvanostatic intermittent titration technique (GITT). The GITT curves were presented in Fig. 3c and the measured ion conductivities as well as the electron conductivities measured by four-point probe were shown in Fig. 3d and Fig. S6. As expected, the Si@LP19 exhibited larger Li-ion diffusion coefficient under all voltages than that of the Si@PEDOT:PSS electrode. The enlarged Li-ion diffusion coefficient may be ascribed to the introduced LiPAA molecules into PEDOT:PSS bulk, which can transfer Li^+ on carboxylic groups with the peristaltic movement of the LiPAA molecules [35]. In addition, the reconstructed molecular configuration caused by the incorporated LiPAA in PEDOT:PSS bulks are possibly beneficial for improving Li-ion diffusion of LP19 binder. As for the electron conductivity, although the mixing of LiPAA decreased the electrical conductivity of PEDOT:PSS (787.4 S cm^{-1}), it is still high enough (675.7 S cm^{-1}) for electron transport [35]. The electrochemical impedance spectroscopy (EIS) was then carried out to investigate the electrochemical kinetics of the electrodes with PEDOT:PSS, LiPAA and LP19 binders cycled at 1.0 A g^{-1} under different cycles and the results are presented in Figs. S7–S9. The EIS curves were fitted employing Zview software and the respective equivalent circuit is presented in Fig. S11. As expected, the EIS spectra presented two semicircles, corresponding to the solid electrolyte interface resistance (R_{SEI}) at high frequency range and charge transfer resistance (R_{ct}) in middle frequency range, respectively [36]. Comparing with those of the Si@LiPAA and Si@PEDOT:PSS electrode, the Si@LP19 showed the smallest R_{SEI} changes from 1.49 Ω at the first cycle to 5.00 Ω after 200 cycles (Fig. 3e), indicating a relative stable SEI layer was formed for Si@LP19 during cycles. Considering that R_{SEI} will emerge rapid degradation in the initial few cycles, we tested the EIS of electrodes with different binders after 1, 3, 5, 7, 9, and 11 cycles (Fig. S10). The first cycle was performed at 0.12 A g^{-1} for charge and discharge, while subsequent cycles were performed at 8.0 A g^{-1}. The results from fitting the EIS curves reaffirm that Si@LP19 exhibits a consistently lower R_{SEI} with minimal fluctuation. This consistency underscores the advantage of LP19 in promoting the formation of stable SEI [37]. The change of R_{ct} for Si@LP19 was also smaller than those of the Si@LiPAA and Si@PEDOT:PSS electrode (Fig. 3f), revealing the fastest electron conduction benefited by the stable conductive molecular network of the LP19 binder. The above results demonstrated the LP19 binder could effectively stabilize the SEI on the Si surface and maintain the electrode integrity, thus guaranteeing the electrochemical properties of electrodes [36]. To certify the advantages of molecular conductive networks, a LED circuit using LP19 binder as wires was assembled as shown in Fig. 3g. It can be seen when the binder wire was cut off, the LED light went out. However, when the broken binder wire was physically touched together gently again, the LED light returned to its original brightness. This proves that although the binder molecule network will break during the charging and discharging process, the electron conductivity will be easily restored due to the double conductive network.

It is well known that the integrity of the electrode structure is tightly related to the cycle stability, thus the electrochemical properties of the Si anode are deeply dependent on the mechanical performances of the binder. Consequently, the nanoindentation test which could simulate the stress caused by the volume change was conducted and the results are presented in Fig. 4a–b. The mechanical strength of the binder was measured under 100 mN. For each sample, 5 indentations were tested to calculate the average value of the hardness and reduced modulus [38]. The Si@PEDOT:PSS shows the highest reduced modulus and hardness, indicating its brittle and fragile characteristics. In contrast, the Si@LP19 presents a moderate hardness and reduced modulus, which is beneficial for accommodation of the stress and maintain the structural integrity during large volume expansion of electrodes [39]. The tensile experimental was then conducted to further investigate the mechanical properties. As shown in Fig. 4c, the LP19 showed ameliorative mechanical performances, such as appropriate tensile strength and strain at break, which are beneficial for relieving the internal stress from volume change of Si particles as well as making pulverized Si particles coalesced together without disintegration during cycling. The optimized tensile property can be ascribed to the rearranged molecular networks of the

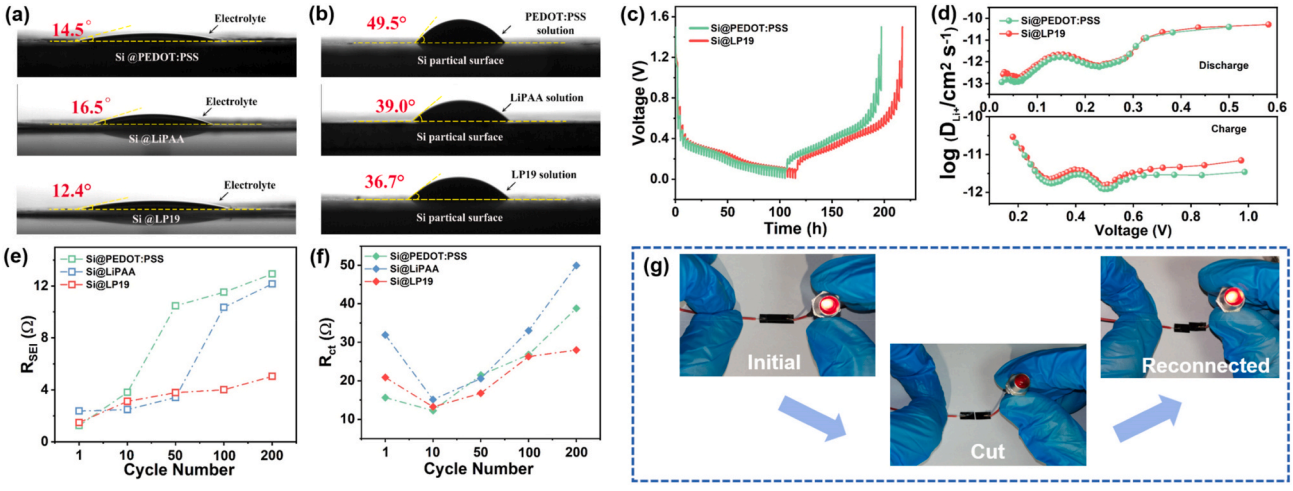

Fig. 3. Characterization of kinetic performance. (a) Digital images for electrolyte contact angle of Si particles composited with PEDOT:PSS, LiPAA, and LP19 binders. (b) Digital images for contact angle of different binders with Si particles. (c) Voltage versus time curve for GITT of Si@PEDOT:PSS, Si@LiPAA, and Si@LP19 electrodes. (d) Li^+ diffusion coefficients at different state during charge/discharge. (e) R_{SEI} and (f) R_{ct} of Si@PEDOT:PSS, Si@LiPAA, and Si@LP19 electrodes with various cycling. (g) The LED circuit using LP19 binder as wires.

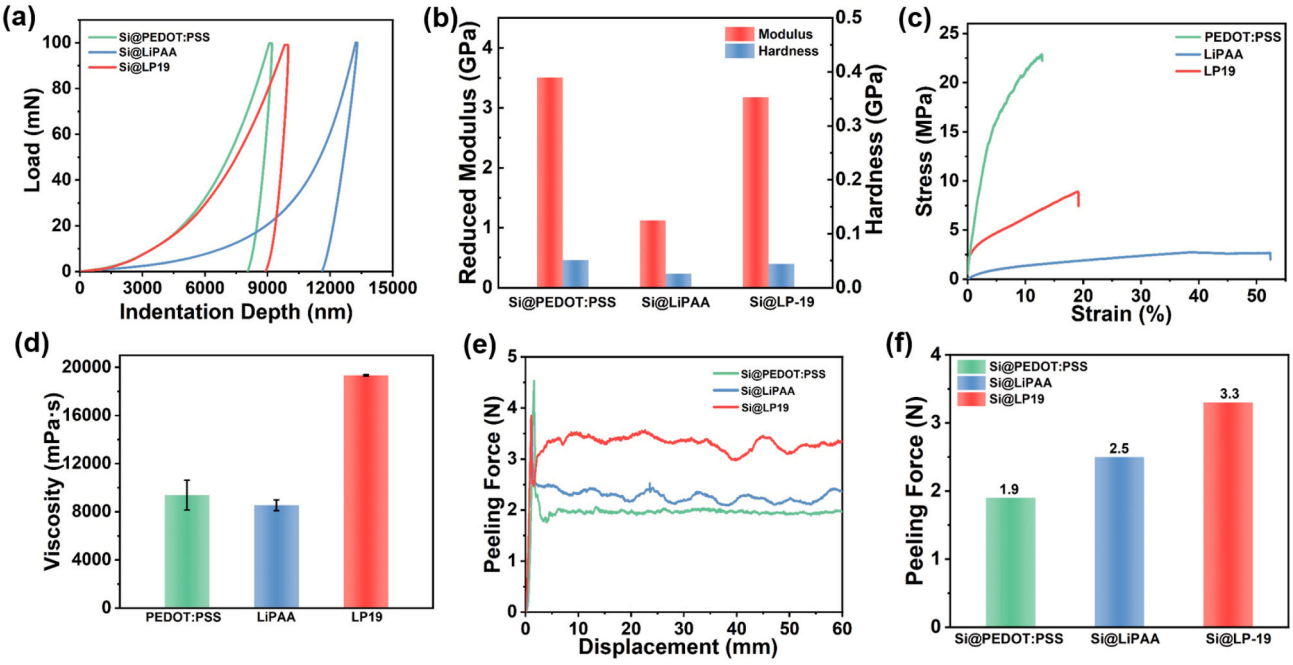

Fig. 4. Characterization of Mechanical performance. (a) The load-displacement curves of Si@PEDOT:PSS, Si@LiPAA, and Si@LP19 electrodes. (b) The reduced modulus and hardness. (c) The stress-strain curves of PEDOT:PSS, LiPAA, and LP19 films. (d) Viscosities of different binder solution (1 wt%). (e) 180° peeling curves and (f) average peeling force of electrodes.

LP19, which composed of energy-dissipating long-range PEDOT:PSS and LiPAA molecules. As shown in Fig. S12, pure PEDOT:PSS depicted an intense characteristic peak at $2\theta = 25.8°$ with (020) plane. After incorporating the LiPAA molecules, the intensity of the characteristic peak decreased for LP19, demonstrating the crystallinity of PEDOT:PSS was destroyed by the mixed LiPAA. The PEDOT:PSS and LiPAA molecules can coexist homogeneously and behave synergistically attributing to the formed multivalent hydrogen bonds [40]. It is known that the hydrogen bonding effect can greatly increase the viscosity of the solution. The enhanced intermolecular interactions were then verified by viscosity tests and it can be seen in Fig. 4d that the LP19 solution exhibits extraordinarily higher viscosity than LiPAA and PEDOT:PSS solutions, demonstrating stronger interactions between LiPAA and PEDOT:PSS were formed. To visually compare the viscosity of the three solutions, few drops of them were added in three vials. When the vials were flipped, the LP19 solution was tightly stuck on the bottom, while LiPAA and PEDOT:PSS solutions flow to the vial cap side due to the gravity, as shown in Fig. S13. The intermolecular force between the PEDOT:PSS and LiPAA was further demonstrated by FTIR and the results were presented in Fig. S14. The –OH bond shifts to a new wavenumber for LP19, indicating hydrogen bonding interaction takes place in the material [41]. In addition to the mechanical properties of the bulk binder proved by tensile test, the adhesion strength of the binder to the current collector is also a pivotal performance. The adhesion strength was studied by 180° peeling test and the results are presented in Fig. 4e and f. It is noteworthy that the Si@LP19 exhibited the highest peeling strength and the average peeling force is 3.3 N cm^{-1}, far larger than those of Si@LiPAA (2.5 N cm^{-1}) and Si@PEDOT:PSS (1.9 N cm^{-1}). The enhanced adhesion strength should be attributed to the formed hydrogen bonding between LiPAA and PEDOT:PSS molecules in the composite binder. These interactions can lead to a more robust and cohesive structure, resulting in increased peeling forces during mechanical testing. The stronger adhesion was further demonstrated by a folding test and the folding test was conducted 3 times to evaluate the adhesion strength of the Si@LP19 coatings. It can be seen in Fig. S15, delamination phenomenon of active materials or exposed Cu current collector were not observed, demonstrating a superior adhesion capacity of the LP19 binder. The coating uniformity of Si particles by LP19 binders was verified by the EDS elemental map. It can be seen in Fig. S16, the silicon and sulfur elements are evenly distributed on the whole electrode, demonstrating Si nanoparticles was homogeneously coated by the LP19 binder, which is beneficial for electrochemical performances of Si anodes.

The morphology analysis employing Scanning Electron Microscope (SEM) was to monitor the morphology and thickness variations before and after the cycling. By the top-viewed SEM images in Fig. 5a–f, the Si@LP19 electrode maintains a smooth and no-crack morphology after 50 cycles under 1.0 A g^{-1}, preserving a structural integrity. While for the electrodes using PEDOT:PSS and LiPAA as binders, chalking phenomenon or severe cracks could be watched, indicating the disintegration of the electrodes. Although PAA is considered to be a suitable electrode binder for the Si anode, the lithiated PAA has retrogressive mechanical flexibility, resulting in serious structural damage of the electrode (Fig. 5e) [42]. From a cross-sectional perspective, the thickness for Si@LP19, Si@LiPAA and Si@PEDOT:PSS were 17.2 μm, 20.3 μm, and 20 μm, respectively, which are similar before cycling (Fig. S17). However, distinct differences occurred after 50 cycles (Fig. 5g–i). The thicknesses reached 20.9 μm, 38.5 μm, and 35.6 μm for the three binders, which are 21.5%, 89.6% and 78% thicker than the pristine state before cycling. The non-crack morphology and smaller thickness increasement of Si@LP19 electrode after 50 cycles further confirmed that the LP19 binder realize a higher mechanical stability.

Whereafter, the XPS examinations were conducted on the electrode surfaces before and after cycling (50 cycles) to study the effect of different binders on the SEI layer (Fig. 5j-l). For all three Si electrodes with different binders after 50 cycles, a new peak appearing at 290.0 eV in C1s spectra was the characteristic peak of semicarbonate ($ROCO_2Li$) and carbonate (Li_2CO_3), which was originated from decomposition of the electrolyte and acted as the main component of the SEI layer [43]. It means the larger the peak area at around 290.0 eV, the more electrolyte was decomposed. It can be clearly seen that the Si@LP19 shows the smallest peak area at 290.0 eV among the three electrodes, demonstrating less electrolyte was decomposed in Si@LP19. After cycling, two new peaks appearing at 685.0 eV and 687.0 eV represent LiF and

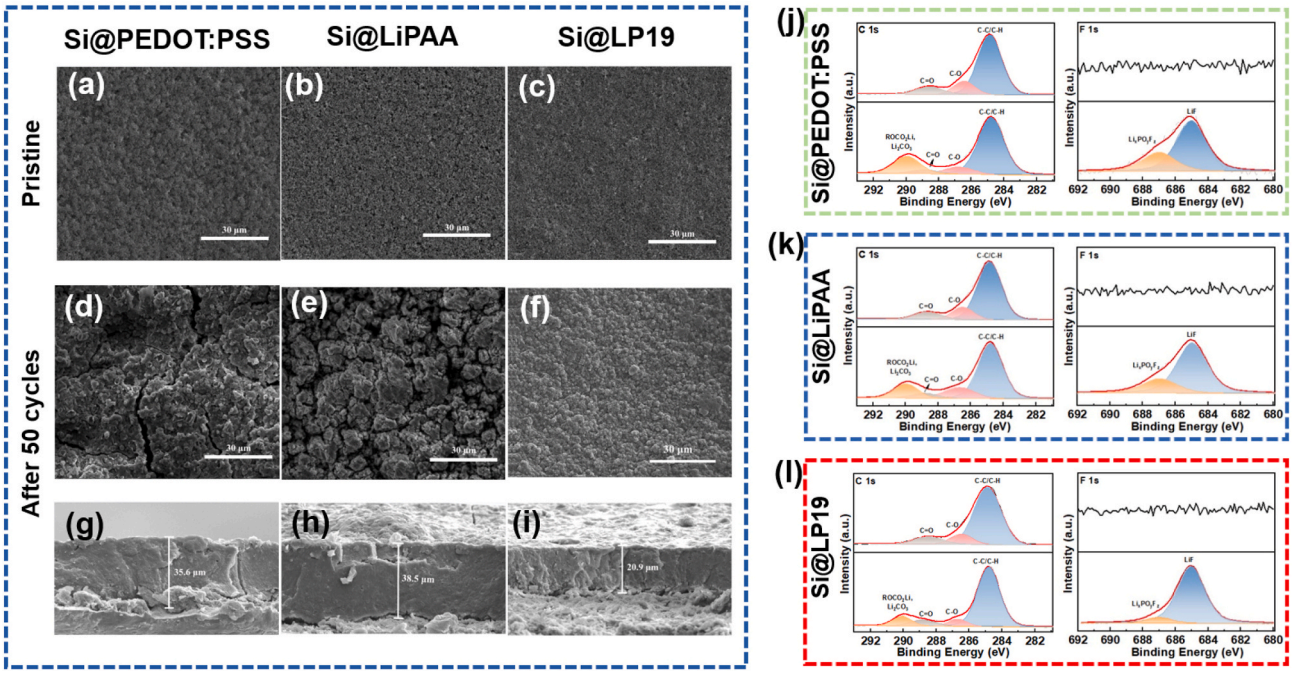

Fig. 5. Post-mortem characterization of electrodes. Top-viewed SEM images of the (a, d) Si@PEDOT:PSS, (b, e) Si@LiPAA, and (c, f) Si@LP19 electrode before and after 50 cycles at 1.0 A g^{-1}. The cross-sectional SEM images of (g) Si@PEDOT:PSS, (h) Si@LiPAA, (i) Si@LP19 after 50 cycles. XPS spectrum of C 1s and F 1s for pristine and cycled (j) Si@PEDOT:PSS, (k) Si@LiPAA, and (l) Si@LP19 electrodes.

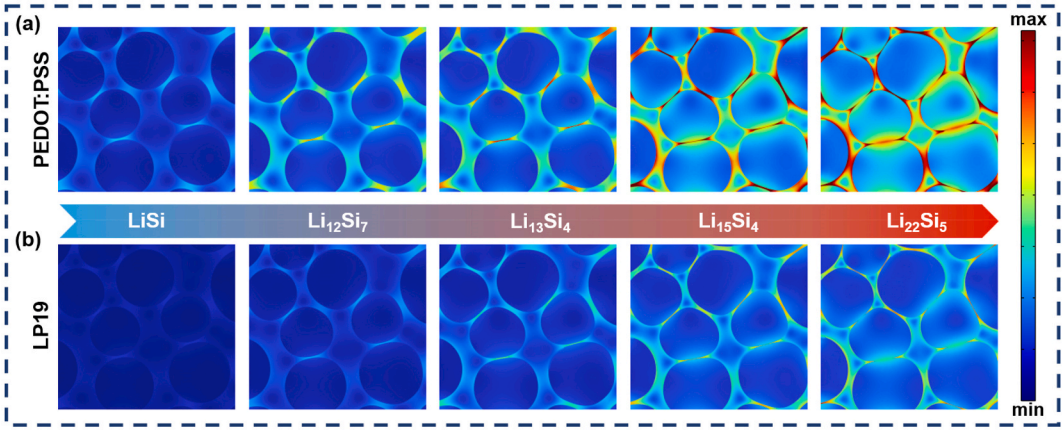

Fig. 6. The finite element method. Stress distribution of Si particles with (a) PEDOT:PSS and (b) LP19 binders at different lithiation states.

$Li_xPF_yO_z$ in F1s spectra, respectively. The $Li_xPF_yO_z$ was caused by the decompositions of $LiPF_6$ and it could adversely affect the electrochemical performances. LiF was a key component of the SEI layer. It possesses low Li^+ diffusion barrier and high shear modulus, which can further avoid excessive consumption of electrolyte due to its stable mechanical performance [44]. The largest LiF peak area of Si@LP19 implying that the LP19 are beneficial to form a stable and thinner SEI, which also prevent the consumption of the electrolytes, thus ensuring the electrochemical performance [45].

To reveal the evolution of stress with different binders during lithiation process, the finite element simulations were carried out. The relevant parameters and phase structures of Si particles during the lithiation process have been utilized (Table S1) [46–48]. Firstly, a random model, in which the spherical Si nanoparticles are distributed in the binder before lithiation is used to capture the typical variations of microstructure and simultaneously reveal the deformation information of Si nanoparticles during lithiation processes. Normally, Si particles will suffer large volume expansions with the continuous intercalation of Li^+, which will cause unavoidable stress concentration. As shown in Fig. 6, the randomly distributed Si nanoparticles incorporated in hard and brittle binder, such as PEDOT:PSS present a severe stress concentration during the whole lithiation process, which would cause failure of the electrode. While the electrode with LP19 binder maintains a relatively low contact stress even at a large lithiation state. The distinct difference between the stress evolutions of the Si anode can be ascribed to the different mechanical behavior of the binder. The PEDOT:PSS demonstrated a stiffness of crystalline polymer while the LP19 demonstrated a proper stress as proved in the tensile stress test. Therefore, the LP19 is more capable to alleviate the stress concentration and ameliorate the long cycling stability of the Si anodes.

3. Conclusions

In summary, we synthesized a multifunctional binder by assembling the LiPAA and highly conductive PEDOT:PSS. This binder simultaneously possesses high electric conductivity, high ion conductivity as

well as optimized mechanical performances. The working mechanism includes three points: 1) the lithiation treatment of PAA is conducive to the transport of lithium ions, 2) the double conductive network constructed by conductive PEDOT:PSS and Super P guarantees the stable electric connectivity during lithiation and delithiation processes, 3) the optimization of the internal configuration of the molecules realizes the structural and cycling stability of the anode. As a consequence, the Si anode utilizing this binary conductive binder demonstrated pronounced cycling stability (2165 mAh g^{-1} after 200 cycles) and rate performance (1315 mAh g^{-1} at 8 A g^{-1}). This strategy will also promote the development of the next generation of high-energy-density LIBs.

4. Methods

Materials. Polyacrylic acid (PAA, MW = 450,000), lithium hydroxide powder (LiOH) and Si with particle size of 60–100 nm were purchased from Shanghai Aladdin Bio-Chem Technology Co., LTD. PEDOT:PSS was obtained from Shanghai Ouyi Electronic Materials. The commercial Si/C materials (1000 mAh g^{-1}) was provided by BTR New Material Group Co., LTD. Super P and electrolyte (LB-046) were purchased from Suzhou Zhongyan Chemical Techology Co., LTD.

Binder Synthesis. 1 g PAA powder was dissolved in 19 g deionized water under a vigorous stirring for 12 h to get a 5 wt% PAA solution. Then, LiOH solutions (10 wt%) were mixed with the above-obtained PAA solution for achieving a partially lithiated PAA binder (The molar ratio of LiOH to acrylic acid is 0.75:1, the name of the mixture is abbreviated as LiPAA). In the end, quantitative LiPAA solution was poured into the PEDOT:PSS solution and the mixture was further stirred vigorously for 12 h at room temperature to form a uniformly cross-linked polymer binder. The resultants were named as LPxy, where the L represents the LiPAA, P represents the PEDOT:PSS, x and y represent the proportions of L and P, respectively.

Electrode Preparation. Si powder, super P, and binders with a mass ratio of 6:2:2 was dispersed into deionized water. The mixture was vigorously stirred overnight at room temperature to form a homogeneous slurry. Then the obtained slurry would be cast onto the copper current collector using a doctor blade with a gap height of 150 μm (the mass loading of Si was approximately 0.8 mg cm^{-2}), followed by drying at 100 °C for 12 h.

Electrochemical measurement. CR2025 coin cells were assembled in an argon-filled glove box. To test electrochemical performance, a galvanostatic charge-discharge cycling test was conducted in a Neware battery test system with potential window controlled between 0.01 V and 1.5 V at 30 °C. The GITT test, which could assess the Li^+ diffusion coefficient during charge and discharge, was evaluated in a Neware battery test system under 0.01–1.5 V based on Fick's second law calculations:

$$D_{Li+} = \frac{4}{\pi\tau}\left(\frac{m_B V_B}{M_B S}\right)^2 \left(\frac{\Delta E_S}{\Delta E_\tau}\right)^2$$

where τ denotes the pulse duration, m_B denotes the active mass, M_B and V_B denote the molar mass and volume, and S denotes the electrode's effective surface area, respectively. ΔE_S and ΔE_τ stand for the voltage change between steps and the voltage change during a pulse cycle, respectively. Here, the electrode's effective surface area is 1.53 cm^2, the relaxation period is 30 min, and the current density is 0.12 A g^{-1}. Cyclic voltammetry (CV) tests and electrochemical impedance analysis (EIS) were carried out using an electrochemical workstation CHI 660 and CHI 760 (Chenhua). Among them, the potential window of CV test is 0.01–1.5 V, and the sweep speed is 0.05 mV s^{-1}. EIS was tested in the frequency ranging from 100 kHz to 10 mHz.

Performance measurement. The surface and cross-sectional morphologies of electrodes before and after cycling were determined by scanning electron microscopy (SEM, JEOL JSM–6700 F). The Fourier transform infrared spectroscopy (FTIR, PerkinElmer) was employed to determine the molecular structures in the range of 4000–400 cm^{-1}. The contact angle was measured utilizing a contact angle system (Dataphysics OCA25). In summary, suitable-sized samples were prepared as test substrates for the electrolyte and positioned on a flat loading platform. Subsequently, the electrolyte was transferred into a contact angle syringe. The contact angle measurements were conducted at room temperature (25 °C), capturing images of the droplet deposition process to assess the electrolyte's wettability towards the negative electrode under investigation. Finally, the software automatically processed these images to analyze and determine the contact angle. X-ray diffraction (XRD, Bruker D8 ADVANCE) was used to characterize the physical structure of PEDOT:PSS, LiPAA and LP19 binder. The viscosity of the binders was tested by a rotational viscometer (Shanghai Changji NDJ-8S). In order to test the mechanical adhesion force of binders, 180° peel tests were conducted using a universal test machine (Instron 3343). Briefly, the electrode was firstly cut into 5cm × 2 cm long strip shape, and the copper foil surface was fixed in stainless steel with 3 M double-sided tape. The 3 M tape was then adhered to the active material surface of the electrode and pressed three times with a 500 N weight roller to ensure that they were tightly bonded. Then, the stainless-steel sheet and 3 M tape were attached to the two clamps, keeping them at 180° and setting the peeling speed at 15 mm min^{-1} for testing. The load-displacement curve was measured by the nanoindenter (Anton Paar NHT^3) with a Berkovich diamond indenter to characterize the mechanical properties of the electrode on the nanometer scale. X-ray photon spectroscopy (XPS, PHI ADEPT 1010) was used to detect the composition of electrode sheet. The electron conductivities of the PEDOT:PSS and LP19 binder films were measured by a digital four probe tester (ST2263) with a pin-distance of about 1 mm.

Finite Element Simulation. In the finite element simulation of the random model, without considering conductive additives, the randomly dispersed Si particles of various sizes within the binder can be regarded as a classic example of two-phase composite materials. During the lithiation process, the increase in lithium intercalation induces compression and expansion of adjacent Si particles, invariably resulting in stress concentration. The distinct difference between of the stress distribution can be ascribed to the different mechanical properties of the binders.

CRediT authorship contribution statement

Wenhui Geng: Formal analysis, Investigation, Writing – original draft, Writing – review & editing. **Xinmeng Hu:** Data curation, Investigation. **Qinhua Zhou:** Data curation, Methodology. **Yinhang Zhang:** Funding acquisition, Supervision, Writing – original draft. **Bin He:** Funding acquisition, Investigation. **Zhiliang Liu:** Funding acquisition, Supervision. **Kuikui Xiao:** Supervision. **Dong Cai:** Supervision. **Shuo Yang:** Conceptualization, Formal analysis. **Huagui Nie:** Validation, Visualization. **Zhi Yang:** Data curation, Funding acquisition, Supervision, Validation.

Declaration of competing interest

The authors declare that they have no known competing financial interests or personal relationships that could have appeared to influence the work reported in this paper.

Data availability

The data that has been used is confidential.

Acknowledgement

This research was supported by the National Natural Science Foundation of China (Grant No. 52302045, 51972238, U21A2081), the Basic Scientific Research Projects of Wenzhou City (Grant No. G20220018) and the Major Talent Engineering Team Project of Wenzhou City (Ouyue

Project).

Appendix A. Supplementary data

Supplementary data to this article can be found online at https://doi.org/10.1016/j.jpowsour.2024.234285.

References

[1] J. Xie, Y.C. Lu, A retrospective on lithium-ion batteries, Nat. Commun. 11 (2020), https://doi.org/10.1038/s41467-020-16259-9.

[2] M.S. Balogun, H. Yang, Y. Luo, W. Qiu, Y. Huang, Z.Q. Liu, Y. Tong, Achieving high gravimetric energy density for flexible lithium-ion batteries facilitated by core-double-shell electrodes, Energy Environ. Sci. 11 (2018) 1859–1869, https://doi.org/10.1039/c8ee00522b.

[3] O.A. Kuznetsov, S. Mohanty, E. Pigos, G. Chen, W. Cai, A.R. Harutyunyan, High energy density flexible and ecofriendly lithium-ion smart battery, Energy Storage Mater. 54 (2023) 266–275, https://doi.org/10.1016/j.ensm.2022.10.023.

[4] Z. Cao, X. Zheng, Q. Qu, Y. Huang, H. Zheng, Electrolyte design enabling a high-safety and high-performance Si anode with a tailored electrode–electrolyte interphase, Adv. Mater. 33 (2021) 1–11, https://doi.org/10.1002/adma.202103178.

[5] N. Zhou, Y. Wu, Y. Li, J. Yang, Q. Zhou, Y. Guo, M. Xia, Z. Zhou, Interconnected structure Si@TiO2-B/CNTs composite anode applied for high-energy lithium-ion batteries, Appl. Surf. Sci. 500 (2020) 1–9, https://doi.org/10.1016/j.apsusc.2019.144026.

[6] X. Han, L. Gu, Z. Sun, M. Chen, Y. Zhang, L. Luo, M. Xu, S. Chen, H. Liu, J. Wan, Y. B. He, J. Chen, Q. Zhang, Manipulating charge-transfer kinetics and a flow-domain LiF-rich interphase to enable high-performance microsized silicon-silver-carbon composite anodes for solid-state batteries, Energy Environ. Sci. 16 (2023) 5395–5408, https://doi.org/10.1039/d3ee01696j.

[7] L. Gu, J. Han, M. Chen, W. Zhou, X. Wang, M. Xu, H. Lin, H. Liu, H. Chen, J. Chen, Q. Zhang, X. Han, Enabling robust structural and interfacial stability of micron-Si anode toward high-performance liquid and solid-state lithium-ion batteries, Energy Storage Mater. 52 (2022) 547–561, https://doi.org/10.1016/j.ensm.2022.08.028.

[8] Z. Sun, M. Li, Z. Zheng, Z. Chen, H. Zhang, B. Xiao, B. Qu, B. Jiang, H. Liao, L. Zhang, M. Li, Q. Zhang, M.S. Wang, Cycle-stable Si-based composite anode for lithium-ion batteries enabled by the synergetic combination of mixed lithium phosphates and void-preserving F-doped carbon, Mater Today Nano 22 (2023) 1–11, https://doi.org/10.1016/j.mtnano.2023.100322.

[9] B.S. Lee, J. Yoon, C. Jung, D.Y. Kim, S.Y. Jeon, K.H. Kim, J.H. Park, H. Park, K. H. Lee, Y.S. Kang, J.H. Park, H. Jung, W.R. Yu, S.G. Doo, Silicon/carbon nanotube/BaTiO3 nanocomposite anode: evidence for enhanced lithium-ion mobility induced by the local piezoelectric potential, ACS Nano 10 (2016) 2617–2627, https://doi.org/10.1021/acsnano.5b07674.

[10] L. Zhao, Y.B. He, C. Li, K. Jiang, P. Wang, J. Ma, H. Xia, F. Chen, Y. He, Z. Chen, C. You, F. Kang, Compact Si/C anodes fabricated by simultaneously regulating the size and oxidation degree of Si for Li-ion batteries, J Mater Chem A Mater 7 (2019) 24356–24365, https://doi.org/10.1039/c9ta09255b.

[11] T. Kohler, E. Hadjixenophontos, Y. Joshi, K. Wang, G. Schmitz, Reversible oxide formation during cycling of Si anodes, Nano Energy 84 (2021) 1–9, https://doi.org/10.1016/j.nanoen.2021.105886.

[12] S. Mei, S. Guo, B. Xiang, J. Deng, J. Fu, X. Zhang, Y. Zheng, B. Gao, P.K. Chu, K. Huo, Enhanced ion conductivity and electrode–electrolyte interphase stability of porous Si anodes enabled by silicon nitride nanocoating for high-performance Li-ion batteries, J. Energy Chem. 69 (2022) 616–625, https://doi.org/10.1016/j.jechem.2022.02.002.

[13] M. Liu, H. Gao, G. Hu, K. Zhu, H. Huang, Facile preparation of core-shell Si@Li4Ti5O12 nanocomposite as large-capacity lithium-ion battery anode, J. Energy Chem. 40 (2020) 89–98, https://doi.org/10.1016/j.jechem.2019.02.011.

[14] J. Bae, D.S. Kim, H. Yoo, E. Park, Y.G. Lim, M.S. Park, Y.J. Kim, H. Kim, High-performance Si/SiOx nanosphere anode material by multipurpose interfacial engineering with black TiO2-x, ACS Appl. Mater. Interfaces 8 (2016) 4541–4547, https://doi.org/10.1021/acsami.5b10707.

[15] X. Han, Z. Zhang, G. Zheng, R. You, J. Wang, C. Li, S. Chen, Y. Yang, Scalable engineering of bulk porous Si anodes for high initial efficiency and high-areal-capacity lithium-ion batteries, ACS Appl. Mater. Interfaces 11 (2019) 714–721, https://doi.org/10.1021/acsami.8b16942.

[16] D. Sui, Y. Xie, W. Zhao, H. Zhang, Y. Zhou, X. Qin, Y. Ma, Y. Yang, Y. Chen, A high-performance ternary Si composite anode material with crystal graphite core and amorphous carbon shell, J. Power Sources 384 (2018) 328–333, https://doi.org/10.1016/j.jpowsour.2018.03.008.

[17] C.-Z. Ke, F. Liu, Z.-M. Zheng, H.-H. Zhang, M.-T. Cai, M. Li, Q.-Z. Yan, H.-X. Chen, Q.-B. Zhang, Boosting lithium storage performance of Si nanoparticles via thin carbon and nitrogen/phosphorus co-doped two-dimensional carbon sheet dual encapsulation, Rare Met. 40 (2021) 1347–1356, https://doi.org/10.1007/s12598.

[18] D. Xie, S. Hu, D. Teng, J. Ma, B. Wang, M. Zhu, Non-noble Si NWs@ZnO core–shell heterojunction anode enables a photo-assisted mirco direct methanol fuel cell, Chem. Eng. J. 457 (2023) 1–9, https://doi.org/10.1016/j.cej.2023.141310.

[19] H. Li, H. Li, Y. Lai, Z. Yang, Q. Yang, Y. Liu, Z. Zheng, Y. Liu, Y. Sun, B. Zhong, Z. Wu, X. Guo, Revisiting the preparation progress of nano-structured Si anodes toward industrial application from the perspective of cost and scalability, Adv. Energy Mater. 12 (2022) 1–25, https://doi.org/10.1002/aenm.202102181.

[20] W. Jang, S. Kim, Y. Kang, T. Yim, T.H. Kim, A high-performance self-healing polymer binder for Si anodes based on dynamic carbon radicals in cross-linked poly (acrylic acid), Chem. Eng. J. 469 (2023) 1–12, https://doi.org/10.1016/j.cej.2023.143949.

[21] X. Liu, J. Zai, A. Iqbal, M. Chen, N. Ali, R. Qi, X. Qian, Glycerol-crosslinked PEDOT:PSS as bifunctional binder for Si anodes: improved interfacial compatibility and conductivity, J. Colloid Interface Sci. 565 (2020) 270–277, https://doi.org/10.1016/j.jcis.2020.01.028.

[22] L. Hu, M. Jin, Z. Zhang, H. Chen, F. Boorboor Ajdari, J. Song, Interface-adaptive binder enabled by supramolecular interactions for high-capacity Si/C composite anodes in lithium-ion batteries, Adv. Funct. Mater. 32 (2022) 1–9, https://doi.org/10.1002/adfm.202111560.

[23] Z. Zheng, H. Gao, C. Ke, M. Li, Y. Cheng, D.L. Peng, Q. Zhang, M.S. Wang, Constructing robust cross-linked binder networks for silicon anodes with improved lithium storage performance, ACS Appl. Mater. Interfaces 13 (2021) 53818–53828, https://doi.org/10.1021/acsami.1c14907.

[24] Y.M. Zhao, F.S. Yue, S.C. Li, Y. Zhang, Z.R. Tian, Q. Xu, S. Xin, Y.G. Guo, Advances of polymer binders for silicon-based anodes in high energy density lithium-ion batteries, InfoMat 3 (2021) 460–501, https://doi.org/10.1002/inf2.12185.

[25] A.N. Preman, H. Lee, J. Yoo, I.T. Kim, T. Saito, S.K. Ahn, Progress of 3D network binders in silicon anodes for lithium ion batteries, J Mater Chem A Mater 8 (2020) 25548–25570, https://doi.org/10.1039/d0ta07713e.

[26] B. Koo, H. Kim, Y. Cho, K.T. Lee, N.S. Choi, J. Cho, A highly cross-linked polymeric binder for high-performance silicon negative electrodes in lithium ion batteries, Angew. Chem. Int. Ed. 51 (2012) 8762–8767, https://doi.org/10.1002/anie.201201568.

[27] Y. Su, X. Feng, R. Zheng, Y. Lv, Z. Wang, Y. Zhao, L. Shi, S. Yuan, Binary network of conductive elastic polymer constraining nanosilicon for a high-performance lithium-ion battery, ACS Nano 15 (2021) 14570–14579, https://doi.org/10.1021/acsnano.1c04240.

[28] J. Pan, G. Xu, B. Ding, Z. Chang, A. Wang, H. Dou, X. Zhang, PAA/PEDOT:PSS as a multifunctional, water-soluble binder to improve the capacity and stability of lithium-sulfur batteries, RSC Adv. 6 (2016) 40650–40655, https://doi.org/10.1039/c6ra04230a.

[29] K.K. Rajeev, E. Kim, J. Nam, S. Lee, J. Mun, T.H. Kim, Chitosan-grafted-polyaniline copolymer as an electrically conductive and mechanically stable binder for high-performance Si anodes in Li-ion batteries, Electrochim. Acta 333 (2020) 1–10, https://doi.org/10.1016/j.electacta.2019.135532.

[30] C. Zhang, Q. Chen, X. Ai, X. Li, Q. Xie, Y. Cheng, H. Kong, W. Xu, L. Wang, M. S. Wang, H. Yang, D.L. Peng, Conductive polyaniline doped with phytic acid as a binder and conductive additive for a commercial silicon anode with enhanced lithium storage properties, J Mater Chem A Mater 8 (2020) 16323–16331, https://doi.org/10.1039/d0ta04389c.

[31] N. Yuca, M.E. Cetintasoglu, M.F. Dogdu, H. Akbulut, S. Tabanli, U. Colak, O. S. Taskin, Highly efficient poly(fluorene phenylene) copolymer as a new class of binder for high-capacity silicon anode in lithium-ion batteries, Int. J. Energy Res. 42 (2018) 1148–1157, https://doi.org/10.1002/er.3913.

[32] E. Bulut, E. Güzel, N. Yuca, O.S. Taskin, Novel approach with polyfluorene/polydisulfide copolymer binder for high-capacity silicon anode in lithium-ion batteries, J. Appl. Polym. Sci. 137 (2020) 1–6, https://doi.org/10.1002/app.48303.

[33] Y. Zhao, L. Yang, Y. Zuo, Z. Song, F. Liu, K. Li, F. Pan, Conductive binder for Si anode with boosted charge transfer capability via n-type doping, ACS Appl. Mater. Interfaces 10 (2018) 27795–27800, https://doi.org/10.1021/acsami.8b08843.

[34] F.H. Du, B. Li, W. Fu, Y.J. Xiong, K.X. Wang, J.S. Chen, Surface binding of polypyrrole on porous silicon hollow nanospheres for li-ion battery anodes with high structure stability, Adv. Mater. 26 (2014) 6145–6150, https://doi.org/10.1002/adma.201401937.

[35] W. Zeng, L. Wang, X. Peng, T. Liu, Y. Jiang, F. Qin, L. Hu, P.K. Chu, K. Huo, Y. Zhou, Enhanced ion conductivity in conducting polymer binder for high-performance silicon anodes in advanced lithium-ion batteries, Adv. Energy Mater. 8 (2018) 1–8, https://doi.org/10.1002/aenm.201702314.

[36] B. Zhang, Y. Dong, J. Han, Y. Zhen, C. Hu, D. Liu, Physicochemical dual cross-linking conductive polymeric networks combining high strength and high toughness enable stable operation of silicon microparticle anodes, Adv. Mater. (2023) 13, https://doi.org/10.1002/adma.202301320.

[37] Q. Li, J. Ruan, S. Weng, X. Zhang, J. Hu, H. Li, D. Sun, X. Wang, F. Fang, F. Wang, Interphasial pre-lithiation and reinforcement of micro-Si anode through fluorine-free electrolytes, Angew. Chem. Int. Ed. 62 (2023) 1–8, https://doi.org/10.1002/anie.202310297.

[38] Z. Li, G. Wu, Y. Yang, Z. Wan, X. Zeng, L. Yan, S. Wu, M. Ling, C. Liang, K.N. Hui, Z. Lin, An ion-conductive grafted polymeric binder with practical loading for silicon anode with high interfacial stability in lithium-ion batteries, Adv. Energy Mater. 12 (2022) 1–12, https://doi.org/10.1002/aenm.202201197.

[39] W. Tang, L. Feng, X. Wei, G. Lai, H. Chen, Z. Li, X. Huang, S. Wu, Z. Lin, Three-dimensional crosslinked PAA-TA hybrid binders for long-cycle-life SiOxAnodes in lithium-ion batteries, ACS Appl. Mater. Interfaces 14 (2022) 56910–56918, https://doi.org/10.1021/acsami.2c19344.

[40] J. Chong, C. Sung, K.S. Nam, T. Kang, H. Kim, H. Lee, H. Park, S. Park, J. Kang, Highly conductive tissue-like hydrogel interface through template-directed assembly, Nat. Commun. 14 (2023) 1–12, https://doi.org/10.1038/s41467-023-37948-1.

[41] Z. Li, Y. Zhang, T. Liu, X. Gao, S. Li, M. Ling, C. Liang, J. Zheng, Z. Lin, Silicon anode with high initial coulombic efficiency by modulated trifunctional binder for high-areal-capacity lithium-ion batteries, Adv. Energy Mater. 10 (2020) 1–11, https://doi.org/10.1002/aenm.201903110.

[42] K.A. Hays, R.E. Ruther, A.J. Kukay, P. Cao, T. Saito, D.L. Wood, J. Li, What makes lithium substituted polyacrylic acid a better binder than polyacrylic acid for silicon-graphite composite anodes? J. Power Sources 384 (2018) 136–144, https://doi.org/10.1016/j.jpowsour.2018.02.085.
[43] X. Lin, Y. Wen, J. Wang, H. Shang, H. Liu, X. Xu, Boston ivy-inspired natural-rich binder with strong adhesion for advanced silicon-based anodes, Chem. Eng. J. 468 (2023) 143784, https://doi.org/10.1016/j.cej.2023.143784.
[44] G.G. Eshetu, E. Figgemeier, Confronting the challenges of next-generation silicon anode-based lithium-ion batteries: role of designer electrolyte additives and polymeric binders, ChemSusChem 12 (2019) 2515–2539, https://doi.org/10.1002/cssc.201900209.
[45] Z. Wu, Z. Wan, Z. Li, Q. Du, T. Wu, J. Cao, M. Ling, C. Liang, Y. Tan, Partially carbonized polymer binder with polymer dots for silicon anodes in lithium-ion batteries, Small 19 (2023) 2205065, https://doi.org/10.1002/smll.202205065.
[46] H. Kim, C.Y. Chou, J.G. Ekerdt, G.S. Hwang, Structure and properties of Li-Si alloys: a first-principles study, J. Phys. Chem. C 115 (2011) 2514–2521, https://doi.org/10.1021/jp1083899.
[47] L. Hu, X. Zhang, P. Zhao, H. Fan, Z. Zhang, J. Deng, G. Ungar, J. Song, Gradient H-bonding binder enables stable high-areal-capacity Si-based anodes in pouch cells, Adv. Mater. 33 (2021) 1–9, https://doi.org/10.1002/adma.202104416.
[48] J. Kim, J. Choi, K. Park, S. Kim, K.W. Nam, K. Char, J.W. Choi, Host–guest interlocked complex binder for silicon–graphite composite electrodes in lithium ion batteries, Adv. Energy Mater. 12 (2022) 1–10, https://doi.org/10.1002/aenm.202103718.